Progress In Electromagnetics Research, Vol. 178, 63–81, 2023

Linear Sampling Method Imaging of Three-Dimensional Conducting Targets from Limited Apertures via Phase-Delay-Constrained Formulations

Matthew Burfeindt* **and Hatim Alqadah**

Abstract—The linear sampling method (LSM) is a qualitative inverse scattering technique for reconstructing the shape of a target. It has several beneficial qualities, including the avoidance of nonlinear optimization and simplified scattering approximations. However, it often struggles when sensors can only be placed on one side of the target. In this paper, we investigate two alternative LSM formulations for overcoming the limited-aspect challenge. The first, the phase-delay frequency variation LSM (PDFV-LSM), incorporates coherent processing across frequency to improve discrimination in the range direction. The second, the phase-encoded LSM (PE-LSM), enhances the PDFV-LSM approach with a receive-beamforming operation to decrease the complexity of the inverse problem. We apply both techniques to simulated data from three-dimensional targets and three-dimensional limited-aspect arrays. We generate three-dimensional reconstructions and compare them to reconstructions from both the conventional LSM and conventional backprojection-based processing. The results demonstrate superior reconstruction fidelity for either the PDFV-LSM, PE-LSM, or both, across a wide variety of imaging scenarios due to finer range resolution. They also demonstrate trade-offs between the two enhanced LSM techniques, with the PE-LSM achieving better range resolution and robustness to noise and the PDFV-LSM achieving better lateral resolution.

1. INTRODUCTION

The reconstruction of perfectly electrically conducting (PEC) or near-PEC targets from scattered electric fields is of interest for a variety of applications, including target identification, classification, and non-destructive evaluation. In principle, the problem may be solved by reconstructing the target dielectric profile via various well-known quantitative inverse scattering techniques (e.g., [1–5]). However, these techniques typically involve iterative nonlinear optimization and significant computational expense. The computational complexity associated with generating a quantitative profile estimate may not be justified for near-PEC targets, as their interior dielectric properties are generally non-informative. In addition, some quantitative techniques may require many iterations or may fail to converge due to the inherent high contrast of PEC or near-PEC material.

These challenges motivate the development of techniques that reconstruct only the shapes and not the dielectric profiles of conducting targets. Various algorithmic strategies have been introduced in the literature. Local shape function and subspace optimization techniques use nonlinear optimization to find a distribution of small conducting elements that approximates the target shape [6–11]. Several techniques use optimization with sparse spatial priors to reconstruct the locations of contrast sources on the target surface [12–16]. Physical-optics-based techniques use high-frequency and linearizing approximations to reduce the complexity of the problem [17–19].

Received 5 April 2023, Accepted 1 September 2023, Scheduled 3 October 2023
* Corresponding author: Matthew Burfeindt (matthew.burfeindt@nrl.navy.mil).
The authors are with the US Naval Research Laboratory, USA.

The linear sampling method (LSM) is a technique for reconstructing target shape that has received significant attention in the literature due to several potential advantages (e.g., [20–33]). The LSM involves solving for a set of transmit weights that focus equivalent currents in the domain [24] as opposed to directly solving for the target shape. The solution may be found with low computational complexity using non-iterative linear optimization. In addition, in its conventional formulation, the LSM requires no use of the Born approximation, and thus has the potential for generating high-fidelity reconstructions even for high-contrast or highly conducting targets.

However, the LSM is generally less effective in limited-aspect scenarios, in which sensors are only placed on one side of the target. Much of the signal information related to the distance of the target to the limited-aspect array, i.e., its range, is found in the change in phase of the signal across frequency. Conventional radar processing strategies, such as backprojection, exploit this phase change for focusing in range. In contrast, the LSM lacks a mechanism for exploiting this phase change. Instead, it finds the solution at each frequency independently and then combines these solutions incoherently. Limited-aspect LSM images may thus appear significantly distorted in the range direction (e.g., [27, 34]). This may limit LSM utility for applications where it may not be possible to view the target from all angles due to constraints on sensor placement. Previous studies have applied various strategies for improving LSM limited-aspect performance, including applying a range-based amplitude weight to the LSM system of equations [26, 28], applying a time-domain LSM implementation [30, 31], regularizing the problem according to a factorization of the far-field operator [32], and using a reciprocity gap functional that requires knowledge of both the electric and magnetic fields [34].

We have previously introduced two LSM variants that incorporate coherent processing across frequencies into their formulation and thus show potential for overcoming the challenges related to limited apertures. The first, the phase-delay frequency-variation LSM (PDFV-LSM), imposes a constraint on the solution across adjacent frequencies in order to encourage a relationship between the solution phase and the signal propagation distance [36, 37]. This effectively incorporates *a priori* propagation information into the optimization that allows for improved reconstruction fidelity. The second, the phase-encoded LSM (PE-LSM), enhances the robustness of the PDFV-LSM formulation via a receive-beamforming step that decreases the complexity of the inverse problem [38, 39]. The techniques maintain the LSM benefit of straightforward implementation by relying on non-iterative linear optimization with L_2 regularization.

In previous studies, we have presented limited-aspect PE-LSM imaging results in two-dimensional (2D) scenarios [38–40]. We have also recently published preliminary three-dimensional (3D) limited-aspect results for the PDFV-LSM in a brief conference paper [37]. There have also been a few previous studies on 3D limited-aperture imaging with other LSM formulations [26, 28, 30, 34]. However, to our knowledge there has not been a comprehensive study of 3D limited-aspect imaging that incorporates coherent processing across frequency into the LSM formulation to improve range resolution. Improved resolution in range is desired both for determining the precise target location and for discriminating between multiple scatterers that may be at different ranges. Reconstruction in 3D necessarily involves an increase in computational expense compared to reconstruction in 2D due to a larger number of spatial locations at which to solve the LSM system of equations. However, it is of interest for extracting richer geometrical information that can be used for more robust evaluation of the target. The scattering dynamics of 3D targets in 3D space are more complex than the 2D scenarios we have previously investigated, and thus it is necessary to validate that the improvements in reconstruction quality we have previously identified in 2D are preserved in 3D scenarios.

In this study, we perform a 3D investigation of both the PDFV- and PE-LSM. We collect simulated data against 3D conducting targets. We generate 3D reconstructions from the simulated data using the PDFV- and PE-LSM and compare the results to reconstructions from the standard LSM and a conventional backprojection approach. The results demonstrate superior reconstruction fidelity by either the PDFV-LSM, the PE-LSM, or both, across a wide variety of imaging scenarios due to finer range resolution. They also demonstrate trade-offs between the two techniques, with the PE-LSM achieving better range resolution and robustness to noise and the PDFV-LSM achieving better lateral resolution. This study is more comprehensive than the preliminary work in [37], which only included a single imaging example and only considered the PDFV-LSM. This new study includes results for both the PDFV- and PE-LSM, uses a wider variety of targets, presents a regularization strategy, and

considers the effects of aperture extent and noise level on the relative performance of the techniques. Thus, it is a significant extension of the previous preliminary work.

There are two primary strategies for distributing sensors across a limited aperture in 3D scenarios. The first involves generating a real aperture by distributing stationary sensors in two directions (e.g., [26, 28, 30, 34]. The second involves mechanically translating a smaller set of sensors across a synthetic aperture (e.g., [26, 27]). The former approach potentially allows for a shorter acquisition time as well as richer data due to the wider variety of multistatic transmit-receive angles. The latter approach uses fewer physical sensors at the expense of a less comprehensive set of multistatic angles and the potential for platform motion errors. In this paper, we use real-aperture arrays in order to leverage the ability of such arrays to focus coherently in 3D. Design and investigation of 3D synthetic-aperture strategies for coherent focusing in all three dimensions via the techniques of interest, including selection of multistatic transceiver geometry and synthetic aperture trajectory, are deserving of their own comprehensive study. We thus leave synthetic aperture processing to future work.

The remainder of this paper is laid out as follows. In Section 2, we describe our formulations for standard LSM, PDFV-LSM, PE-LSM, and backprojection. In Section 3, we present results from simulated data. In Section 4, we summarize the study and make concluding statements.

2. METHOD

2.1. LSM Fundamentals

We assume that an unknown target is situated in 3D space offset from a distribution of N_{tx} transmitters and N_{rec} receivers. In sequence, each transmitter illuminates the target with an incident field, and the resulting scattered field is recorded at each receiver. For ease of explication, we assume that the transmitters and receivers are co-polarized in the $+z$-direction, and thus the recorded scattered field phasor at each frequency of interest is a scalar. Achieving effective imaging using sensors with only a single polarization is of interest for reducing the hardware complexity of the system. For each collected wavenumber k, we collect the scattered field phasors for every transmit-receive antenna combination in the $N_{\text{rec}} \times N_{tx}$ matrix $\mathbf{E}(k)$.

The conventional LSM involves solving a system of linear equations in the form

$$\mathbf{E}(k)\mathbf{g}(k,\mathbf{r}) = \mathbf{\Phi}(k,\mathbf{r}), \tag{1}$$

where $\mathbf{r}$ is a voxel location in the imaging domain, $\mathbf{g}(k,\mathbf{r})$ is the $N_{tx} \times 1$ LSM solution vector, and $\mathbf{\Phi}(k,\mathbf{r})$ is the $N_{\text{rec}} \times 1$ vector of Green's functions between $\mathbf{r}$ and each receiver. In this study, we use a normalized Green's function vector such that

$$\mathbf{\Phi}(k,\mathbf{r}) = \mathbf{\Phi}^0(k,\mathbf{r})/||\mathbf{\Phi}^0(k,\mathbf{r})||, \tag{2}$$

where $\mathbf{\Phi}^0(k,\mathbf{r})$ is the vector of Green's functions for each receiver. The normalization in (2) has been used in previous studies [28, 39] to mitigate the challenge of limited-aspect imaging. We select the standard Green's function in 3D such that the ith component of $\mathbf{\Phi}^0(k,\mathbf{r})$ is given by

$$\Phi^{0,i}(k,\mathbf{r}) = \exp\left(-jkd^i_{\text{rec}}(\mathbf{r})\right)/d^i_{\text{rec}}(\mathbf{r}), \tag{3}$$

where $d^i_{\text{rec}}(\mathbf{r})$ is the ith component of $\mathbf{d}_{\text{rec}}$, defined as the the $N_{\text{rec}} \times 1$ vector of the distances between each receiver and $\mathbf{r}$. Our choice of Green's function is modestly simplified, as due to the vectorial nature of electric fields the pattern generated by an elementary source in 3D includes an angular amplitude variation in addition to the phase delay and range decay present in (3). However, the limited-aspect nature of the arrays in this study limit this angular variation over the array footprints. We have experimented with including the angular variation for all examples in this study based on the expected radiation pattern of a dipole as given in [41] and have verified that effects on image quality are minor. Thus, we use the Green's function given in (3) for simplicity and conciseness.

A Tikhonov-regularized solution to (1) can be computed via

$$\min_{\mathbf{g}(k,\mathbf{r})} ||\boldsymbol{\rho}(k,\mathbf{r})||^2 + \alpha||\mathbf{g}(k,\mathbf{r})||^2, \tag{4}$$

where $\boldsymbol{\rho}(k,\mathbf{r}) = \mathbf{E}_s(k)\mathbf{g}(k,\mathbf{r}) - \mathbf{\Phi}(k,\mathbf{r})$ is the residual vector to (1), and α is a regularization parameter. It can be shown using arguments from mathematics [20] or electromagnetics [24] that a low-norm solution

to (1) can be found if $\mathbf{r}$ is inside the target support, assuming sufficient sensor diversity and density. Conversely, if $\mathbf{r}$ is outside the target support, then the solution norm is expected to grow very large. Thus, a representation of the target support can be generated by solving (1) for each $\mathbf{r}$ in the scene and for all collected k and plotting an indicator function of the solution norm. In this paper, we use a multifrequency indicator function similar to one that has been used in previous limited-aspect LSM studies [26, 28, 39], given by

$$I(\mathbf{r}) = \left(\sum_n \frac{||\mathbf{g}(k_n, \mathbf{r})||^2}{\max_{\mathbf{r}'} ||\mathbf{g}(k_n, \mathbf{r}')||^2} \right)^{-1}, \tag{5}$$

where k_n is the nth collected wavenumber, and the norms are over the transmitters. The normalization of the indicator over $\mathbf{r}'$ has been shown in some cases to improve limited-aspect performance by helping to differentiate the signals in range.

For all standard LSM results in this paper, we include both the Green's function normalization in (2) and the indicator function normalization in (5) that were previously introduced in [26, 28] in order to make the fairest comparison to the state-of-the-art in limited-aspect LSM imaging. For brevity, we do not include standard LSM processing results without these normalizations, as they result in imagery that is either very similar or somewhat degraded relative to results that include the normalization.

The procedure outlined above has several critical benefits. The system to solve in (1) is linear and computationally inexpensive to solve. Furthermore, the preceding treatment does not rely on the Born approximation, and thus the technique in principle has broad applicability with respect to target type. However, the desired solution norm behavior breaks down as sensor angular diversity or spatial density decreases. In particular, limited-aperture performance is hindered by the absence of coherent processing across frequency. Using (4), the LSM solution at each frequency is independent of the solution at all other frequencies. In addition, the indicator given by (5) or other common implementations from the literature [25] is formed by non-coherent summation of each frequency component. Thus, the phase change in the signal across frequency, which contains much of the signal range information, is neglected. Modification of the LSM formulation may thus be required for some sensor geometries in order to recover this information and thereby achieve improved range discrimination.

2.2. PDFV- and PE-LSM

In this subsection, we briefly describe the PDFV- and PE-LSM. More comprehensive treatments can be found in [36, 39]. Both the PDFV- and PE-LSM incorporate coherent processing across frequency via a constraint on the solution for $\mathbf{g}(k, \mathbf{r})$. Let the PDFV constaint vector be given by

$$\boldsymbol{\gamma}(k, \mathbf{r}) = \mathbf{g}(k, \mathbf{r}) - \mathbf{g}(k + \Delta k, \mathbf{r}) \odot \exp(-j\Delta k \mathbf{d}_{tx}(\mathbf{r})), \tag{6}$$

where Δk is the spacing between adjacent collected wavenumbers; $\mathbf{d}_{tx}(\mathbf{r})$ is the $N_{tx} \times 1$ vector of distances between $\mathbf{r}$ and each transmitter; and '$\odot$' represents element-wise multiplication. The PDFV-LSM solution is then found via

$$\min_{\mathbf{g}(k,\mathbf{r})} \sum_i ||\boldsymbol{\rho}(k_i, \mathbf{r})||^2 + \alpha ||\mathbf{g}(k_i, \mathbf{r})||^2 + \beta ||\boldsymbol{\gamma}(k_i, \mathbf{r})||^2, \tag{7}$$

where β is a second regularization parameter. The rationale for the PDFV constraint is related to the perspective of $\mathbf{g}(k, \mathbf{r})$ as a weighting on the transmitters that induces focused equivalent currents in the target [24]. Under the Born approximation, a focused equivalent current distribution also implies a focused incident field distribution. If $\mathbf{g}(k, \mathbf{r})$ successfully focuses the target equivalent currents and thus the incident field at $\mathbf{r}$, then $\mathbf{g}(k + \Delta k, \mathbf{r})$ must compensate for the change in propagation-based phase of the incident field given by $\Delta k \mathbf{d}_{tx}(\mathbf{r})$ in order to maintain the focus. The PDFV constraint in (7) encourages this behavior, which effectively introduces *a priori* information into the inverse problem that mitigates the lack of a full complement of sensor locations.

By linking the solution phase across frequency according to the expected change in propagation phase, the constraint in (6) can also be seen as a strategy to inject coherent processing across frequency into the LSM formulation. It thus potentially improves the range discrimination, and therefore the limited-aspect performance, of the LSM. It is interesting to note that the coherent link between frequencies is enforced when solving (7), while the summation across frequencies via (5) is incoherent.

The PDFV constaint thus affects the amplitude of the LSM solution in order to achieve improved range performance. This differs from conventional backprojection-based processing, wherein the complex signal components are summed coherently in order to take advantage of phase changes across frequency.

In the PE-LSM, the minimization in (7) is modified with a receive-beamforming enhancement such that the solution is found via

$$\min_{\mathbf{g}(k,\mathbf{r})} \sum_i \left|\mathbf{w}_{\text{rec}}^{\text{H}}(k_i,\mathbf{r})\boldsymbol{\rho}(k_i,\mathbf{r})\right|^2 + \alpha||\mathbf{g}(k_i,\mathbf{r})||^2 + \beta||\boldsymbol{\gamma}(k_i,\mathbf{r})||^2, \tag{8}$$

where the superscript 'H' refers to the conjugate transpose, and the receive-beamforming weight vector is defined as

$$\mathbf{w}_{\text{rec}}(k,\mathbf{r}) = \exp(-jk\mathbf{d}_{\text{rec}}(\mathbf{r})). \tag{9}$$

The rationale for this choice is as follows. As described in [39], the beamforming weight vector in (9) focuses the array on receive at the point $\mathbf{r}$. This is due to the phase of the beamforming weights being matched to the electrical path length of the signal between the receivers and $\mathbf{r}$. (This is the frequency-domain analog to the well-known time-reversal focusing operation for a single tone.) We hypothesize that, by emphasizing signal contributions from scattering features near $\mathbf{r}$ and de-emphasizing contributions from features remote from $\mathbf{r}$, this operation reduces the complexity of the solution space. By potentially reducing the degrees of freedom of the solution, i.e., the number of pixels that are emphasized and therefore allowed to significantly contribute to the solution, we stabilize the ill-posed inverse problem in the scenario where the measurements also have limited degrees of freedom due to, for instance, limited-aspect sensors. The results in our previous study in 2D [39] demonstrate empirically the efficacy of combining the PDFV constraint with the receive-beamforming operation. In this study, we are interested in whether these results extend to 3D.

2.3. Backprojection

The designs of the PDFV constraint vector in (6) and the receive-beamforming weight vector in (9) rely on matched propagation-based phases that are similar to those used for spatial matched filtering by conventional backprojection techniques. However, there is a critical difference in the imaging mechanism between these approaches. In the PDFV- and PE-LSM, the matched phases aid in finding a stable solution to the system of equations in (1). The LSM solution behavior, i.e., the difference in the behavior for the solution norm for points inside and outside the target support, is then leveraged to reconstruct the target. In backprojection approaches, the matched phases are used to form the image directly by focusing the data at each pixel in the scene.

It is thus of interest to compare the performances of the PDFV- and PE-LSM to backprojection in order to determine whether LSM-based processing extracts richer target information when the solution is constrained by assumptions derived from matched phases. To this end, we generate a backprojection solution at $\mathbf{r}$ via the transmit-receive focusing operation given by

$$I^{\text{B}}(\mathbf{r}) = \left|\sum_n \mathbf{w}_{\text{rec}}^{\text{H}}(k_n,\mathbf{r})\mathbf{E}(k_n)\mathbf{w}_{tx}^{*}(k_n,\mathbf{r})\right|^2, \tag{10}$$

where

$$\mathbf{w}_{tx}(k,\mathbf{r}) = \exp(-jk\mathbf{d}_{tx}(\mathbf{r})) \tag{11}$$

and '$*$' is the complex conjugate.

3. RESULTS

In this section, we present the results of applying the PE-LSM, PDFV-LSM, standard LSM, and backprojection to simulated data in the 3D limited-aperture geometries of interest. We first describe the simulated data acquisitions in Subsection 3.1. We then describe the procedure for regularization parameter selection in Subsection 3.2. For an example target, we demonstrate the extraction of 2D cross-sectional results from the 3D reconstructions in Subsection 3.3, evaluation of fidelity with quantitative metrics in Subsection 3.4, and visualization of the 3D reconstructions via isosurfaces Subsection 3.5.

We then present more comprehensive results across a variety of targets in Subsection 3.6. Lastly, we demonstrate the effects of varying the array extent and the signal-to-noise ratio (SNR) in Subsections 3.7 and 3.8, respectively.

3.1. Simulated Data

The sensing geometry for this study is illustrated in Fig. 1. We generate simulated data for this geometry via the 3D finite-difference time-domain (FDTD) method. We define a rectangular array geometry as follows. We distribute transmit and receive locations across five lines that run parallel to the x-axis and are equally spaced in the z-direction. For most examples in this study, each line has five receive locations and nine transmit locations, resulting in total sensor counts of $N_{\text{rec}} = 25$ and $N_{tx} = 45$. Unless otherwise specified, the array dimensions are 6×6 m. We place targets offset from the array by 5 m in the $-y$-direction. Based on this array geometry, in this paper we refer to the $-y$-direction as the range direction, the x-direction as the azimuth direction, and the z-direction as the elevation direction.

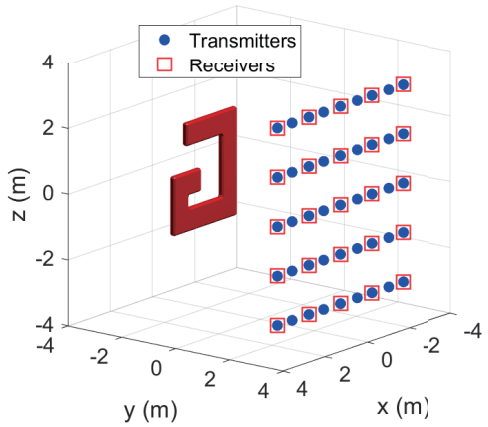

Figure 1. The sensing geometry. Included is an example G-shaped target.

The targets are modeled with electric conductivity of 5.7×10^7 S/m. We choose targets that are of width 0.2 meters in the y-direction but significantly larger in the two lateral dimensions. We make this choice for two reasons. First, the electric fields will not penetrate the highly conducting targets. Given the limited aspect of the array, there is therefore expected to be minimal information on target extent in the y-direction in the scattered field, qnd thus the imaging problem is reduced to reconstructing the illuminated surfaces of the target. Second, choosing targets that are thinner in the range direction highlights the differences in range discrimination between the techniques of interest.

In sequence, we source each transmit location with a z-directed current source. We then collect the z-component of the resulting time-domain scattered fields at each receive location. We use the discrete Fourier transform to convert the time-domain fields to phasors at six frequencies uniformly distributed between 250 and 300 MHz. We add Gaussian white noise to the scattered field phasors prior to each imaging trial. Unless otherwise specified, the resulting signal-to-noise ratio (SNR) measured across all spatial and frequency samples is 20 dB. The noisy scattered field phasors are collected into the data matrices $\mathbf{E}(k)$.

3.2. Regularization Parameter Selection

The PDFV- and PE-LSM both require selection of two regularization parameters. The first, α, penalizes large-norm solutions in the same manner as in conventional Tikhonov regularization. The second, β, penalizes deviations from the phase behavior encouraged by the PDFV constraint in (6). Choosing an appropriate balance between the two penalties is necessary to achieve the best imaging results.

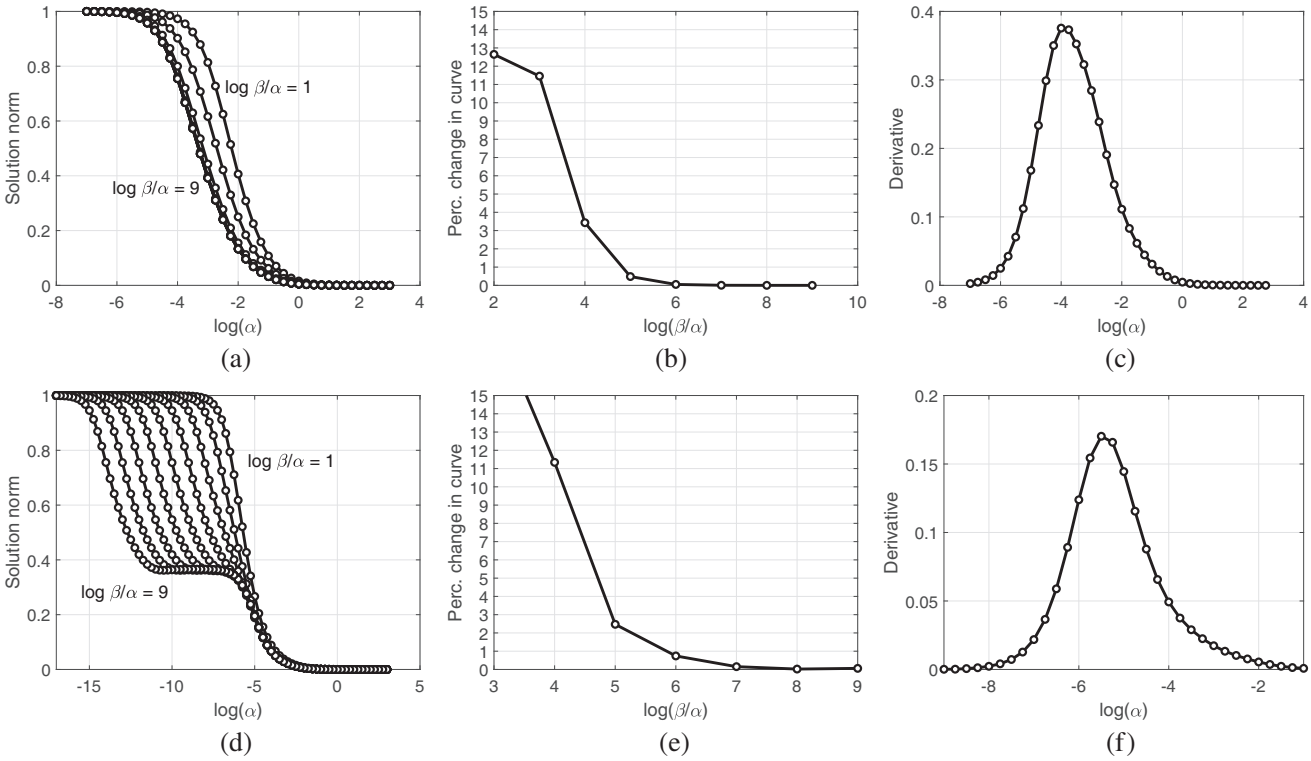

Figure 2. The solution-norm curves used for choosing regularization parameters for the (top row) PE-LSM and (bottom row) PDFV-LSM. (a), (d) η vs. α for varying β/α. (b), (e) The percent change in η vs. β/α. (c), (f) The derivative of the converged η.

Automated heuristics for choosing the the regularization parameter in inverse problems, such as the well-known L-curve method [46], often involve observing the behavior of the solution norm and/or the residual norm as a function of the regularization parameter and identifying inflection points. We have previously introduced and demonstrated a robust method for choosing α and β for the PE-LSM [39] using similar intuition. We adopt the same strategy in this study. For the convenience of the reader, we briefly summarize the strategy in this subsection. Further explication can be found in [39]. We then describe a similar but modestly modified strategy that we have adopted for the first time for the PDFV-LSM.

For both the PDFV- and the PE-LSM, we compute $\mathbf{g}(k, \mathbf{r})$ on a sparse $4 \times 4 \times 4$-cell, $4 \times 4 \times 4$-meter grid of voxels for a wide variety of values of α and β/α. We then compute the following quantity,

$$\eta(\alpha, \beta/\alpha) = \eta_0 \left(\int \int ||\mathbf{g}(k, \mathbf{r}, \alpha, \beta/\alpha)||^2 d\mathbf{r} dk \right)^{1/2}, \tag{12}$$

where η_0 is a scale factor that sets $\eta = 1$ for the lowest choice of α. Computing $\eta(\alpha, \beta/\alpha)$ allows us to determine how the solution-norm behavior changes with the regularization parameters. Example curves for the PE-LSM are plotted in Fig. 2(a) for the G-shaped target illustrated in Fig. 1.

We choose regularization parameters for the PE-LSM using heuristics based on two salient features of the η curves. First, the shape of the η curve converges as β/α increases. Based on this behavior, we choose the ratio β/α at the point of convergence — defined here as a change of less than 1 percent in η after an order of magnitude change in β/α — in order to achieve the greatest influence of the PDFV penalty on the solution. A plot of the percent change in the η curve is shown in Fig. 2(b) for the G-shaped target. According to the heuristic, we choose $\log \beta/\alpha = 5$.

Second, as α is increased from small to large values, the solution norm starts large, goes through a transition region, and then becomes small. Based on this behavior, we choose α at the inflection point of the curve, which we have observed empirically leads to the highest fidelity results. We determine the

inflection point by computing the derivative of the converged η with respect to α and selecting the α that results in the derivative peak. For this example, the heuristic results in $\log \alpha = -4$, as shown in Fig. 2(c).

The η behavior for the PDFV-LSM differs from the PE-LSM, as shown in Fig. 2(d). There are multiple inflection points in the η curve. In addition, convergence with β/α is not achieved over all α. However, convergence is achieved in the vicinity of the inflection point around the larger α value. We therefore modify our heuristic for PDFV-LSM imaging in the following manner. First, we compute convergence taking into account only the portion of the η curve in the vicinity of the higher-α inflection point. In this example, we use the portion of the curve betwen $\log \alpha = -6.75$ and $\log \alpha = -3.25$. As shown in Fig. 2(e), this leads to choosing $\log \beta/\alpha = 6$. Second, we select α according to the peak of the converged derivative in the same portion of the curve. In this example, this leads to a choice of $\log \alpha = -5.5$, as shown in Fig. 2(f).

As given in (4), the conventional Tikhonov-regularized LSM also requires the choice of the single regularization parameter α. In this study, we simply choose α using the "kneedle" implementation [45] of the L-curve strategy. For the examples in this study, we have also swept over a wide range of α to confirm that apparent limited-aperture degradation of the standard LSM results are not due simply to regularization choice.

3.3. Cross-Sectional Results

We first present 2D cross-sections through the 3D reconstructions. Cross-sectional results are plotted in Fig. 3 for the G-shaped target depicted in Fig. 1. Fig. 3(a) shows results for a cross-section parallel to the xz-plane that passes through the illuminated faces of the scatterers. These results demonstrate the ability of the various techniques to resolve features in azimuth and elevation, i.e., the two cross-range directions. The reconstruction for each technique is of reasonable fidelity to the true target cross-sectional geometry, as regions of elevated indicator are concentrated within the lateral target footprint. Some differences are evident between the techniques. For the PDFV-LSM and the standard LSM, the peak indicator responses are narrower, and thus the indicators are more concentrated within the target footprint compared to the PE-LSM and backprojection. The PDFV-LSM and the standard LSM thus appear to achieve somewhat finer cross-range resolution.

Figure 3(b) shows cross-sections parallel to the yz-plane that run through the top and bottom horizontal arms of the G-shaped target. Thus, they demonstrate the relative performance of each technique for resolving features in the range direction (i.e., the $-y$-direction). These results show a much more significant difference in imaging performance across the four techniques. The PE-LSM clearly achieves the best resolution in the range direction, with the areas of high indicator value well-concentrated within the true scatterer footprint. The PDFV-LSM achieves good but modestly poorer resolution. Standard LSM and backprojection achieve significantly lower range resolution. However, the backprojection image energy is centered on the true target location, whereas the standard LSM indicator is off-center from the target in the $-y$-direction. The standard LSM therefore arguably achieves the worst range performance.

3.4. Fidelity Metrics

While visual inspection is critical for evaluating the imaging performance of the techniques of interest, we can gain additional context and confidence in our evaluations by quantifying performance via appropriate metrics. We quantify fidelity using variations of the well-known Jaccard index which has been used in previous qualitative inverse scattering studies [35, 43, 44]. The conventional Jaccard index can be expressed as

$$J(P, I_\gamma(\mathbf{r})) = \frac{I_\gamma(P) \cap T(P)}{I_\gamma(P) \cup T(P)}, \tag{13}$$

where $I_\gamma(\mathbf{r})$ is a binary representation of the indicator $I(\mathbf{r})$ formed by applying a threshold at value γ, $T(\mathbf{r})$ the true target support, and P a set of voxels over which to perform the computation. However, as seen in Fig. 3, the techniques of interest have distinct performances depending on whether the image cross-range or range characteristics are being considered. In addition, we have found that the

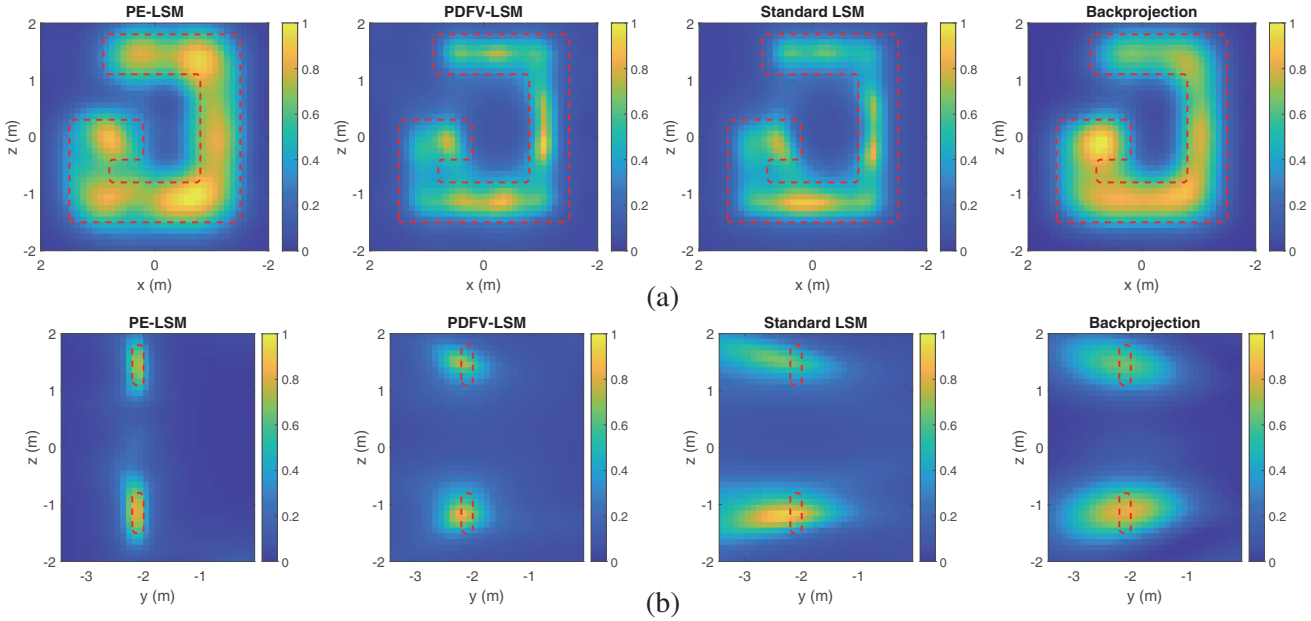

Figure 3. Cross-sections through 3D reconstructions for each technique of interest for the G-shaped target. (a) Cross-sections through the illuminated faces of the scatterers. (b) Cross-sections cutting through the targets in the direction of wave propagation. Each image is normalized to the value of the most intense voxel in the corresponding 3D reconstruction.

conventional Jaccard index is dominated by the range performance for the techniques for the scenarios in this study. Thus, using a single index to characterize imaging performance results in some loss of context and nuance.

We therefore use two modified versions of the Jaccard index for this study. We refer to the first as the cross-range index, as it is intended to quantify the ability of the techniques to resolve features in the cross-range directions. We define it as

$$J_C = J(P_C, I_\gamma(\mathbf{r})), \tag{14}$$

where P_C is the set of all voxels which have the same y-coordinate as any point in the target support. Thus, J_C is essentially the Jaccard index applied only over cross-sections parallel to the xz-plane that contain the target. Likewise, we refer to the second index as the range index, as it is intended to quantify the ability of the techniques to resolve in the range direction. We define it as

$$J_R = J(P_R, I_\gamma(\mathbf{r})), \tag{15}$$

where P_R is the set of all voxels which have the same $x-$ and z-coordinates as any point in the target support. We can thus see J_R as the Jaccard index applied over every line in the y-direction that passes through the target support. Both J_C and J_R output values ranging from 0 to 1, with higher values corresponding to higher-fidelity reconstructions.

We plot J_C and J_R across a range of thresholds for the G-shaped target and for each of the four techniques of interest in Fig. 4(b). The threshold γ reported in the plots is normalized according to the maximum voxel intensity in each image. The cross-range index plot shows that each of the four methods reaches a similar peak J_C value for γ between 0.2 and 0.4. This is consistent with the visual appearance of the imagery in Fig. 3(a), in which each method gives a reasonable representation of the lateral target shape. The somewhat higher γ required for the PE-LSM to achieve peak J_C is also consistent with its modestly lower apparent cross-range resolution in Fig. 3(a). As resolution coarsens, higher γ is required to minimize the number of above-threshold voxels that are outside the target support.

In contrast, the range index plot shows significant differences in peak J_R, with the PE-LSM by far having the best performance, followed in order by the PDFV-LSM, backprojection, and the standard LSM. These results are also consistent with the visual appearance of the images given in Fig. 3(b) and discussed in Subsection 3.3.

3.5. Visualization of 3D Results

We visualize the target reconstruction in 3D space by displaying an isosurface that is defined by the voxel locations at which the indicator crosses a desired threshold γ. However, the γ at which to define the isosurfaces is not obvious. As can be seen in the results in Section 3.4, the γ that results in the best range discrimination may differ from the γ that results in the best cross-range discrimination. The best γ may also depend on the method used for image formation.

For a given reconstruction, we select the γ for 3D visualization in the following manner. We compute the J_C and J_R curves as in Fig. 4(b). We identify the γ that results in the peak J_C and the peak J_R and select the mean of these two values. The rationale for this approach is to provide a compact representation that evinces both the range and cross-range features of the reconstruction. Our aim for displaying the isosurfaces in this manner is to allow straightforward visual evaluation of the differences in reconstruction across the four methods under investigation. Selecting the best image thresholds when the true target geometry is unknown is an interesting problem [33] that is outside the scope of this study.

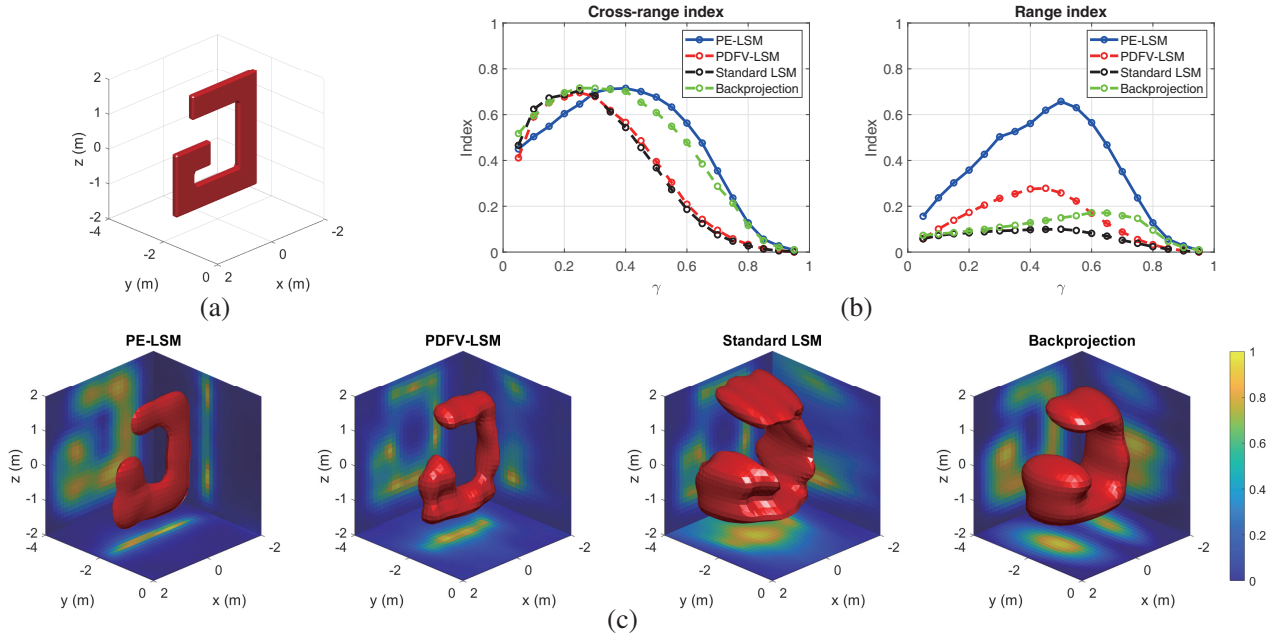

Figure 4. Reconstruction results for the G-shaped target. (a) The true target support. (b) The cross-range and range fidelity indices for each method as a function of threshold γ. (c) The isosurface representation of the 3D reconstruction of each method superimposed over orthogonal cross-sections through the 3D reconstruction.

The isosurfaces generated for the G-shaped target are plotted in Fig. 4(c). The true target support is also plotted in Fig. 4(a) at the same viewing angle in order to provide a straightforward comparison. Each isosurface is superimposed on three orthogonal cross-sections of the corresponding 3D reconstruction to provide additional context. We select cross-sections that pass through the most intense voxel.

The isosurface plots for each method are consistent with the results in Subsections 3.3 and 3.4. Each reconstruction evinces good fidelity to the shape of the target in the cross-range directions. The PE-LSM isosurface is somewhat broader in the lateral dimensions compared to the PDFV-LSM isosurface, which is in accord with the visual appearance of the indicator functions in Fig. 3(a) and the differences in J_C peak locations in Fig. 4(b). Much more significant differences are apparent in the extents of the isosurfaces in the y-direction. The PE-LSM isosurface is the thinnest, followed by the PDFV-LSM and then the backprojection and standard LSM isosurfaces. This result is again consistent with the apparent differences in range resolution across the four techniques as discussed in Subsections 3.3 and 3.4.

3.6. Results for a Variety of Targets

Next, we present cross-sections, isosurfaces, and fidelity metrics for reconstructions from a wider variety of targets. Fig. 5 shows results for a target comprising two uneven bars at different range and elevation offset positions. Fig. 6 shows results for a target comprising a large rectangle and a smaller square. The square is positioned such that it partially shadows the rectangle. The uneven bar target scene and the rectangle and square target scene are of interest for demonstrating the ability of the techniques to resolve scatterers at multiple ranges. Fig. 7 shows results for three small squares placed in a non-symmetric arrangement. Lastly, Fig. 8 shows results for a bullseye target. These latter two scenes are of interest for demonstrating the ability of the techniques to discriminate in cross-range between multiple non-connected scatterers.

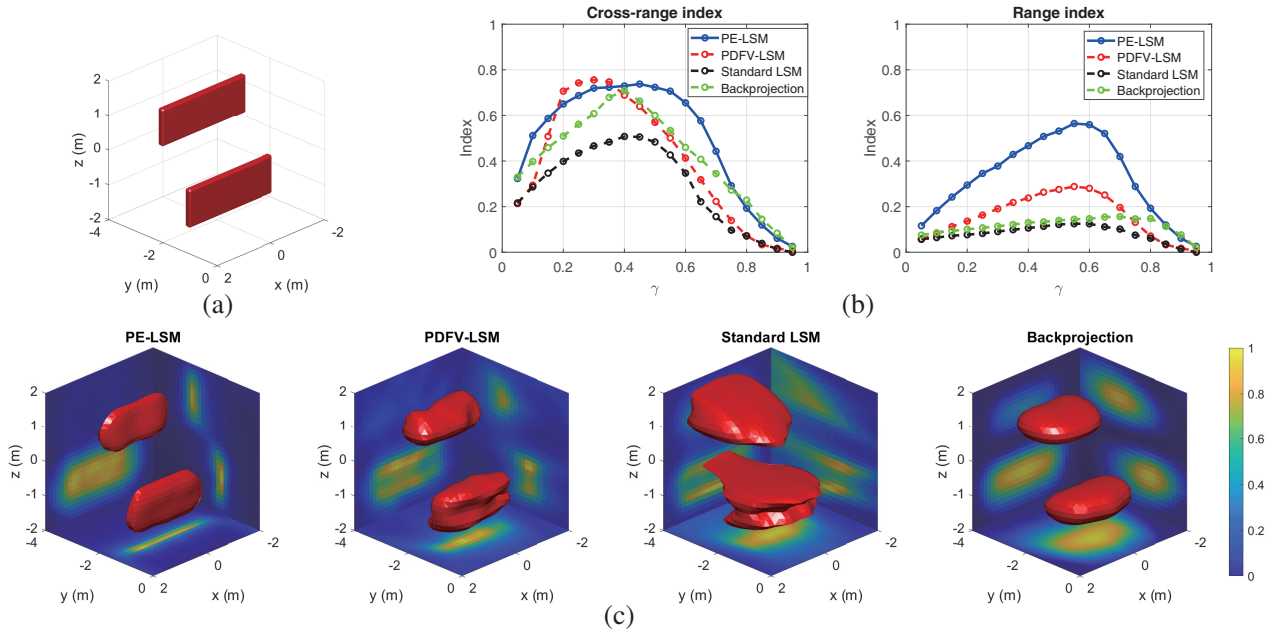

Figure 5. Reconstruction results for the uneven bars target. (a) The true target support. (b) The cross-range and range fidelity indices for each method as a function of threshold γ. (c) The isosurface representation of the 3D reconstruction of each method superimposed over orthogonal cross-sections through the 3D reconstruction.

As in Fig. 4, the PE-LSM consistently achieves the best range resolution across the four targets in this subsection, while the PDFV-LSM also achieves good but modestly coarser range resolution. In some cases, the PDFV-LSM also evinces slightly worse distortions in target shape in range. This effect can be observed in the shape of the top uneven bar in the cross-section parallel to the yz-plane in Fig. 5. The standard LSM and backprojection techniques show much coarser range resolution. The range degradation for the standard LSM is particularly significant for the upper uneven bar in Fig. 5 and the rectangle in Fig. 6. For the latter case, the target is arguably not resolved in range at all, such that the relative positions of the two scatterers in the scene are difficult to discriminate in the y-direction via the isosurfaces.

The apparent cross-range performance across the four targets is also consistent with the the results in Fig. 4. Each method generally creates a reasonable lateral reconstruction of the target faces. In a few cases, finer cross-range detail is apparent in the PDFV-LSM reconstruction compared to the PE-LSM reconstruction. In Fig. 6, the corners of the rectangle are sharper in the PDFV-LSM cross-section parallel to the xz-plane. In Fig. 8, the central disc is more separated from the outer ring in the PDFV-LSM reconstruction. These results are consistent with the interpretation that the PDFV-LSM achieves somewhat finer cross-range resolution compared to the PE-LSM.

The behavior of the quantitative fidelity metrics support these visual interpretations of

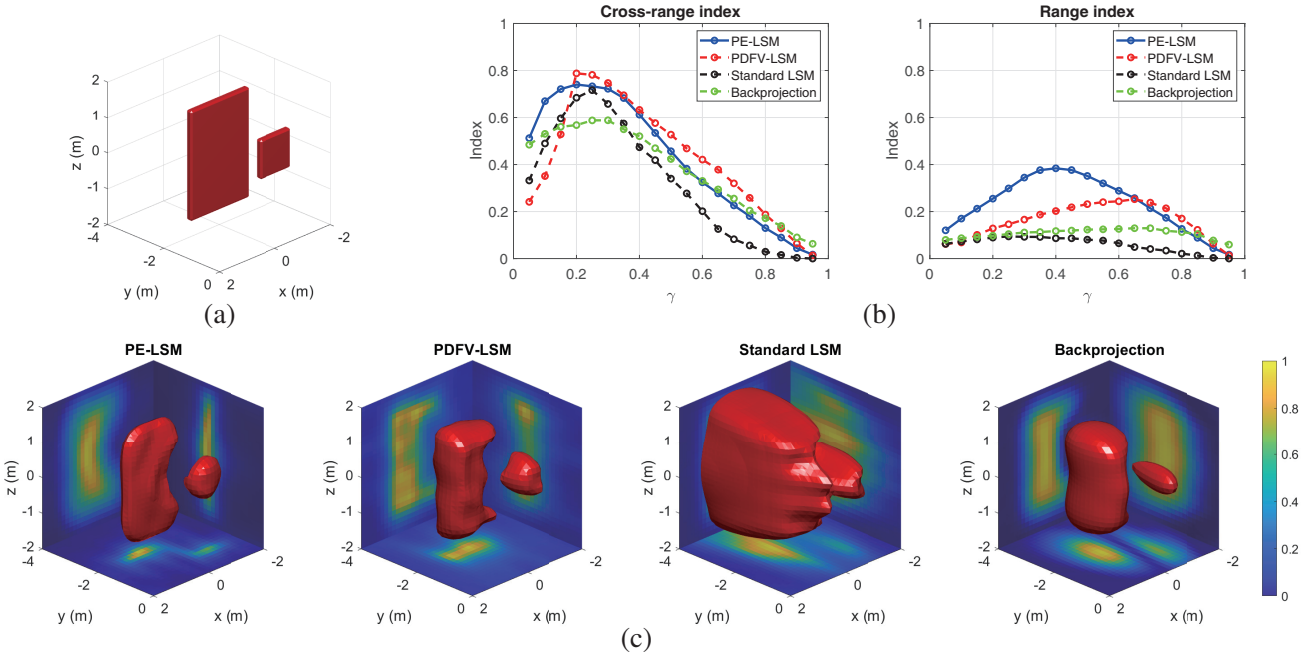

Figure 6. Reconstruction results for the rectangle-and-square target. (a) The true target support. (b) The cross-range and range fidelity indices for each method as a function of threshold γ. (c) The isosurface representation of the 3D reconstruction of each method superimposed over orthogonal cross-sections through the 3D reconstruction.

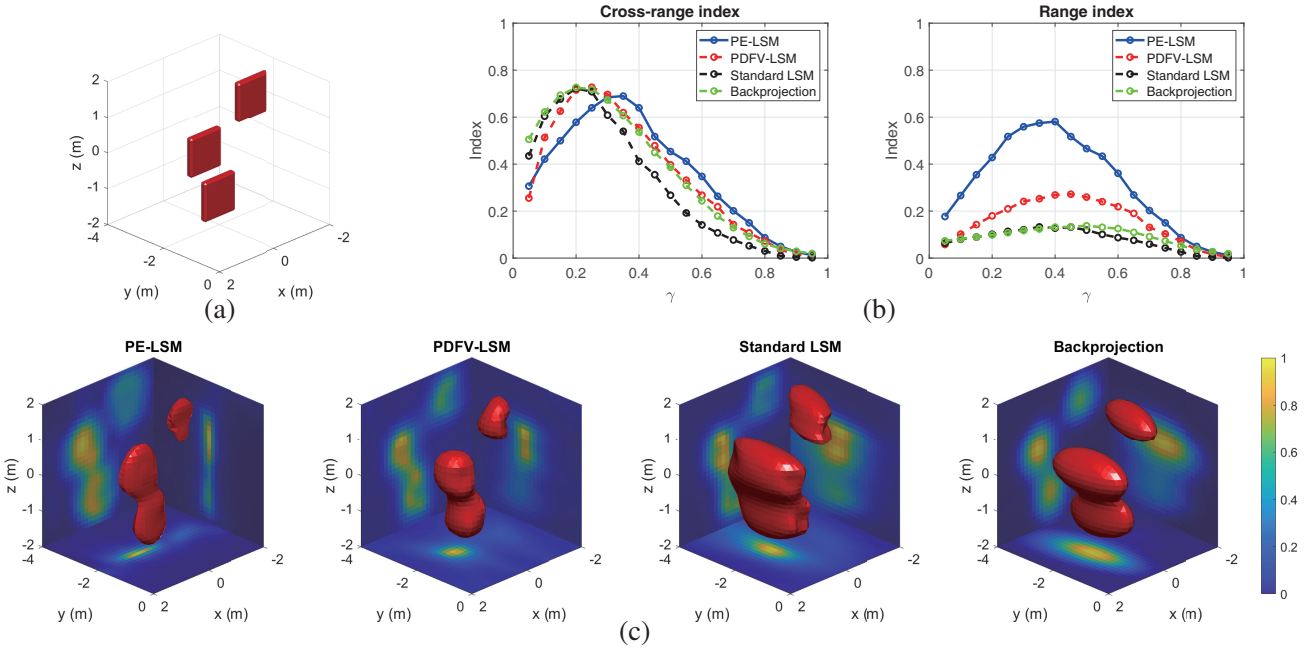

Figure 7. Reconstruction results for the three-square target. (a) The true target support. (b) The cross-range and range fidelity indices for each method as a function of threshold γ. (c) The isosurface representation of the 3D reconstruction of each method superimposed over orthogonal cross-sections through the 3D reconstruction.

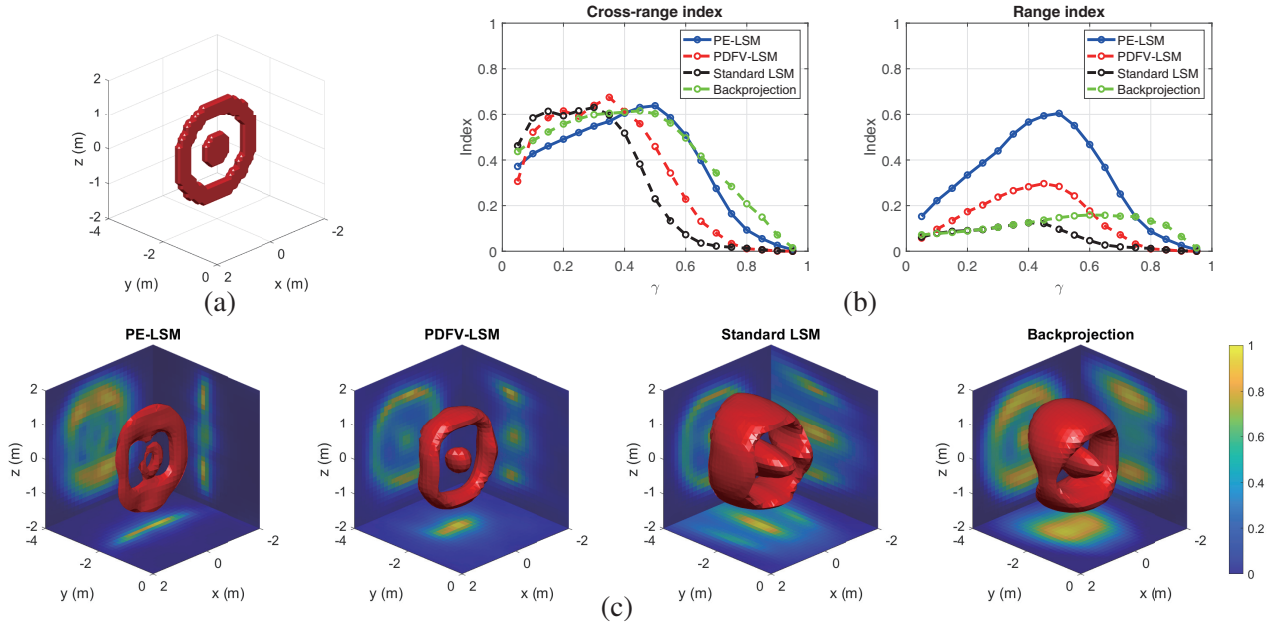

Figure 8. Reconstruction results for the bullseye target. (a) The true target support. (b) The cross-range and range fidelity indices for each method as a function of threshold γ. (c) The isosurface representation of the 3D reconstruction of each method superimposed over orthogonal cross-sections through the 3D reconstruction.

reconstruction quality. The PE-LSM has much higher peak J_R than the other techniques across all four targets. The peak J_C is typically similar across the techniques with a few differences in some cases. The PDFV-LSM achieves somewhat higher peak J_C in each case compared to the PE-LSM. This may related to the finer lateral detail in PDFV-LSM reconstructions noted above. The standard LSM has a significantly lower peak J_C in Fig. 5 compared to the other methods. This is most likely caused by range leakage of the closer bar into the plane of the second bar due to the very poor range resolution of the standard LSM.

3.7. Effects of Aperture Extent

In this subsection, we explore the robustness of the four techniques to changes in the extent of the sensor aperture. In Fig. 9 we plot cross-sectional results for a scenario where the dimensions of the array described in Section 3.1 are reduced from 6×6 m to 4×4 m. The number of transmit and receive locations is kept constant. We plot cross-sections of the 3D reconstructions in order to provide a direct and straightforward evaluation of resolution compared to the cross-sectional results in Fig. 3.

Degradation in cross-range fidelity is evident for all four techniques to some extent in Fig. 9(a). The degradation is minimal for the PDFV-LSM and the standard LSM. For the standard LSM, the indicator is lower in portions of the target footprint. The lateral degradation is more significant for the PE-LSM and backprojection. For these two techniques, the apparent shape of the indicator has lost some lateral definition and there has been some leakage of indicator outside the target footprint.

Range degradation is minimal for the PE-LSM, PDFV-LSM, and backprojection in Fig. 9(b). This is consistent with expectations, as these three methods use coherent processing across frequencies, which allows for range discrimination without wide sensor apertures. As in Fig. 3, the PE-LSM achieves the best range discrimination across the four techniques with the smaller array. Overall, the differences in resolution between the PE-LSM and the PDFV-LSM — that is, better range discrimination with the former and better cross-range discrimination for the latter — are consistent with effects demonstrated in Figs. 4–8.

In contrast to the other three methods, the range degradation of the standard LSM has worsened considerably compared to Fig. 3, as the target responses have stretched further behind the target. The

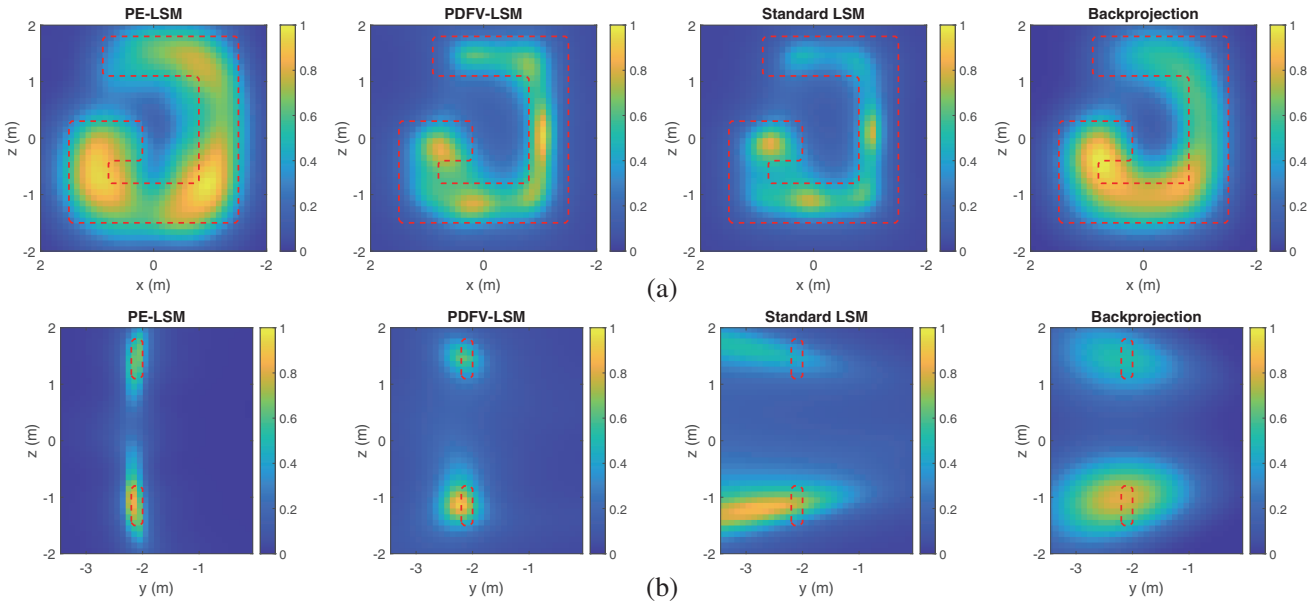

Figure 9. Cross-sections through 3D reconstructions of the G-shaped target for a smaller sensor array. (a) Cross-sections through the illuminated faces of the scatterers. (b) Cross-sections cutting through the targets in the direction of wave propagation. Each image is normalized to the value of the most intense voxel in the corresponding 3D reconstruction.

standard LSM relies on signal changes across sensor position for range discrimination due to its lack of a mechanism for coherent processing across frequencies, and thus poorer range resolution with a narrower array is consistent with expectations.

3.8. Noise Performance

Lastly, we consider the effects of lowering the SNR from the 20 dB value used in the previous subsections. In Figs. 10(a) and 10(b), we plot reconstructions for SNRs of 10 dB and 0 dB, respectively, for the G-shaped target. The results show that the four techniques vary in their robustness to noise level. The backprojection results are the least sensitive to noise level, with minimal changes observed between Figs. 4(c), 10(a), and 10(b). This is consistent with expectations due to the large gain of signal over noise resulting from beamforming on both transmit and receive via (10). The PE-LSM results also evince robustness to noise, with minimal degradation for 10 dB SNR and a modest blurring in the range direction for 0 dB SNR. Similar to backprojection, the apparent robustness of the PE-LSM to noise is most likely due to the receive beamforming operation in (8). The modestly higher sensitivity to noise for the PE-LSM in comparison to backprojection may be due to beamforming only on receive with the former as opposed to on both transmit and receive for the latter.

In contrast, both the standard LSM and the PDFV-LSM evince less robustness to noise. The standard LSM reconstruction degrades significantly in both range resolution and contrast with the background as SNR decreases. The PDFV-LSM moderately degrades in range resolution for 10 dB SNR and completely loses reconstruction fidelity for 0 dB SNR.

3.9. Discussion

For each example in Subsections 3.3–3.8, the highest-fidelity reconstruction results are achieved by either the PE-LSM or the PDFV-LSM. Incorporating coherent processing across frequencies into the solution leads to fundamental improvements in range discrimination compared to the standard LSM in the limited-aperture scenarios of interest. In addition, the PDFV-LSM and PE-LSM also outperform conventional backprojection processing in range discrimination. This outcome is interesting,

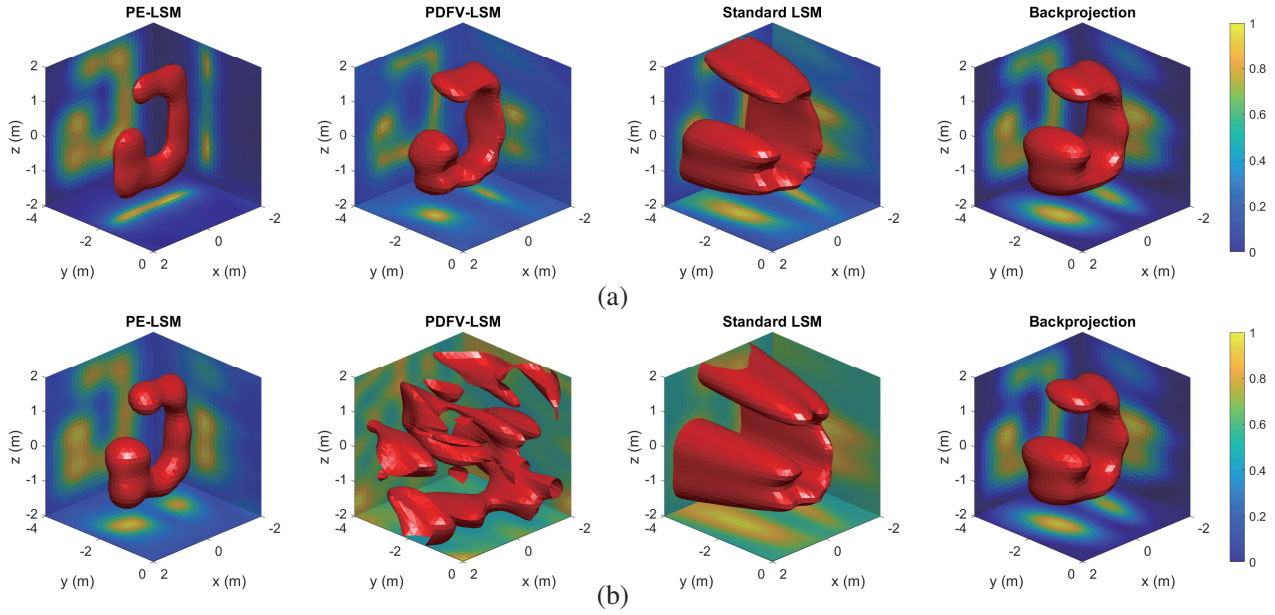

Figure 10. Reconstruction results for lower SNRs of (a) 10 dB and (a) 0 dB.

as backprojection also leverages coherent multi-frequency processing for range focusing. The improved performance may be due to the similarity of LSM-based processing to spectrum estimation techniques such as MUSIC [29] and minimum-variance distortionless-response (MVDR) beamforming [42], which generally achieve better resolution compared to matched-filtering-based techniques.

The results in this study suggest strengths of the PE-LSM and PDFV-LSM relative to alternative strategies for 3D limited-aspect LSM imaging. The standard LSM results in this study include the Green's function normalization in (2) and the indicator function normalization across $\mathbf{r}'$ in (5) which were introduced in [26, 28]. Thus, the improved range resolution of the PE-LSM and PDFV-LSM for these cases demonstrates their advantage over range weighting of the LSM solution alone. The results also suggest potential advantages over time-domain LSM implementations for these geometries. As described in [30], time-domain LSM imaging results are expected to achieve results of similar fidelity as the standard multifrequency LSM for data processed over similar bandwidths. To our knowledge, there is thus no indication from the previous literature that time-doman LSM implementations are capable of achieving the high range resolutions of our proposed techniques. Lastly, the PE-LSM and the PDFV-LSM are advantageous relative to the technique in [34] as they require only knowledge of the electric field and not the magnetic field. Requiring knowledge of both fields, as in [34], would require additional hardware complexity.

The results also suggest several trade-offs in performance between the PDFV-LSM and the PE-LSM. The PE-LSM consistently achieves better range discrimination and is significantly more robust to higher noise levels. The PDFV-LSM often achieves better cross-range image definition, especially as the sensor aperture size decreases. These outcomes suggest that the best choice between the PDFV-LSM and the PE-LSM is scenario-dependent, with practical considerations such as the available sensor footprint, the scattering cross-section of the target, and the availability of low-noise amplifiers being critical variables. Alternatively, in some scenarios the two techniqes could be used in concert. Forming one higher-range-resolution image with the PE-LSM and one higher-cross-range-resolution with the PDFV-LSM could provide the user with the most context for evaluating the unknown target geometry. The low computational expense of the LSM-based techniques compared to other inverse scattering techniques that use nonlinear optimization supports the practicality of forming multiple images in a given sensing scenario. Future work thus may involve adapting the proposed techniques in order to simultaneously achieve the benefits of both the PDFV-LSM and the PE-LSM. A promising approach may be to modify the weight design in (9) to achieve higher angular resolution in the receive beamformer and therefore higher cross-range resolution for the PE-LSM.

This paper proposes the PE-LSM and the PDFV-LSM for limited-aspect imaging of conducting targets. While their performance against dielectric targets is not within the scope of this study, it is of interest to make a few comments on potential limitations. The techniques include compromises with the Born approximation. The system of equations in (1) that forms the basis for the standard, PE-, and PDFV-LSM requires no Born approximation. However, the PDFV constraint in (6) and the beamformer weight design in (9) are Born approximated. As shown in [39], applying the PE-LSM to a purely dielectric target in a limited-aspect configuration may result in artifacts. The PDFV constraint and the beamformer weight design do not take into account the change in wave speed inside the target, and thus the reflections off the target back wall may cause areas of high indicator function to appear behind the target. We refer the reader to [39] for further discussion on this topic. To overcome this challenge, future work may include applying the concepts underpinning the PE-LSM and the PDFV-LSM to hybrid schemes in the style of [47, 48] for joint shape and electrical properties reconstruction for dielectric targets or for imaging in heterogeneous backgrounds for applications such as subsurface imaging, medical imaging, or airport passenger screening for hidden objects.

This paper establishes the theoretical feasibility of PE-LSM and PDFV-LSM processing in 3D for the real-aperture arrays of interest to this study. Unfortunately, to our knowledge there are no publicly available experimental datasets for inverse scattering development that are relevant to the array geometries of interest — that is, real apertures with densely sampled frequencies to enable coherent processing across frequency without range ambiguities. For example, the existing 3D experimental dataset made available by the Fresnel Institute [49] only includes receivers along a single arc and includes only wide frequency spacings (250 MHz steps). Acquisition of experimental data and experimental validation of the proposed techniques are thus significant steps that we leave for future work.

4. CONCLUSION

In this paper, we investigated the performance of two LSM-based imaging techniques in limited-aperture scenarios against 3D conducting targets. The two techniques, the PDFV-LSM and the PE-LSM, are formulated to achieve better range discrimination than standard LSM processing via the incorporation of coherent processing across frequency. They maintain a principal benefit of LSM processing in requiring only linear optimization and low computational complexity. We generated imagery from simulated data for a variety of target shapes, aperture extents, and SNRs and processed the data with the PDFV-LSM, the PE-LSM, the standard LSM, and conventional backprojection. Across all examples, the best imaging results were achieved by either the PDFV-LSM or the PE-LSM due to their significantly improved range resolution. We demonstrated interesting trade-offs between the PE-LSM and the PDFV-LSM. The PE-LSM was shown to achieve the best range resolution and robustness to noise, while the PDFV-LSM generally achieved better cross-range resolution. The results demonstrate the promise of using phase-delay-constrained LSM formulations for imaging scenarios where the target cannot be completely surrounded by sensors due to practical constraints.

ACKNOWLEDGMENT

This work was supported by the Office of Naval Research via the NRL 6.2 Base Program.

REFERENCES

1. Chew, W. C. and Y. M. Wang, "Reconstruction of two-dimensional permittivity distribution using the distorted Born iterative method," *IEEE Trans. Med. Imag*, Vol. 9, No. 2, 218–225, 1990.
2. Wang, Y. M. and W. C. Chew, "An iterative solution of the two-dimensional electromagnetic inverse scattering problem," *Int. J. Imag. Syst. Technol.,* Vol. 1, No. 1, 100–108, 1989.
3. Cui, T. J. and W. C. Chew, "Inverse scattering of two-dimensional dielectric objects buried in a lossy Earth using the distorted Born iterative method," *IEEE Trans. Geosci. Remote Sens.*, Vol. 39, No. 2, 339–346, 2001.

4. Van den Berg, P. M. and A. Abubakar, "A contrast source inversion method," *Inverse Problems*, Vol. 13, 1607–1620, 1997.
5. Gilmore, C., P. Mojabi, and J. LoVetri, "Comparison of an enhanced distorted born iterative method and the multiplicative-regularized contrast source inversion method," *IEEE Trans. Ant. Prop.,* Vol. 57, No. 8, 2341–2351, 2009.
6. Poli, L., G. Oliveri, and A. Massa, "Imaging sparse metallic cylinders through a local shape function Bayesian compressive sensing approach," *Journal of the Optical Society of America*, Vol. 30, No. 6, 1261–1272, 2013.
7. Takenaka, T., Z. Q. Meng, T. Tanaka, and W. C. Chew, "Local shape function combined with genetic algorithm applied to inverse scattering for strips," *Microw. Opt. Technol. Lett*, Vol. 16, 337–341, 1997.
8. Otto, G. P. and W. C. Chew, "Microwave inverse scattering — local shape function imaging for improved resolution of strong scatterers," *IEEE Trans. Microw. Theory Technol.*, Vol. 42, No. 1, 137–141, 1994.
9. Ye, X., "Electromagnetic imaging of wave impenetrable objects," *Proc. 11th Eur. Conf. Antennas Propag.*, 1421–1428, Paris, France, 2017.
10. Ye, X., Y. Zhong, and X. Chen, "Reconstructing perfectly electric conductors by the subspace-based optimization method with continuous variables," *Inverse Problems*, Vol. 27, No. 55011, 2011.
11. Shen, J., Y. Zhong, X. Chen, and L. Ran, "Inverse scattering problems of reconstructing perfectly electric conductors with TE illumination," *IEEE Trans. Antennas Propag.*, Vol. 61, No. 9, 4713–4721, Sep. 2013.
12. Bevacqua, M. and T. Isernia, "Shape reconstruction via equivalence principles, constrained inverse source problems and sparsity promotion," *Progress In Electromagnetic Research*, Vol. 158, 37–48, 2017.
13. Bevacqua, M. and R. Palmeri, "Qualitative methods for the inverse obstacle problem: A comparison on experimental data," *Journal of Imaging*, Vol. 5, No. 4, 47, 2019.
14. Stevanovic, M., L. Crocco, A. Djordjevic, and A. Nehorai, "Higher order sparse microwave imaging of PEC scatterers," *IEEE Transactions on Antennas and Propagation*, Vol. 64, No. 3, 988–997, 2016.
15. Vojnovic, N., M. Stevanovic, L. Crocco, and A. Djordjevic, "High-order sparse shape imaging of pec and dielectric targets using TE polarized fields," *IEEE Transactions on Antennas and Propagation*, Vol. 66, No. 4, 2035–2043, 2018.
16. Nikolic, M. M., A. Nehorai, and A. R. Djordjevic, "Electromagnetic imaging of hidden 2-D PEC targets using sparse-signal modeling," *IEEE Trans. Geosci. Remote Sens.*, Vol. 51, No. 5, 2707–2721, 2013.
17. Wang, F. F. and Q. H. Liu, "A Bernoulli-Gaussian binary inversion method for high-frequency electromagnetic imaging of metallic reflectors," *IEEE Trans. Antennas Propag.*, Vol. 68, No. 4, 3184–3193, 2020.
18. Soldovieri, F., A. Brancaccio, G. Leone, and R. Pierri, "Shape reconstruction of perfectly conducting objects by multiview experimental data," *IEEE Trans. Geosci. Remote Sens.,* Vol. 43, No. 1, 65–71, 2005.
19. Solimene, R., A. Buonanno, F. Soldovieri, and R. Pierri, "Physical optics imaging of 3-D PEC objects: Vector and multipolarized approaches," *IEEE Trans. Geosci. Remote Sens.*, Vol. 48, No. 4, 1799–1808, 2010.
20. Cakoni, F., D. Colton, and P. Monk, *The Linear Sampling Method in Inverse Scattering Theory.* Society for Industrial and Applied Mathematics, Philadelphia, 2011.
21. Colton, D., H. Haddar, and M. Piana, "The linear sampling method in inverse electromagnetic scattering theory," *Inverse Problems*, Vol. 19, S105–S137, 2003.
22. Cakoni, F. and D. Colton, "The linear sampling method for cracks," *Inverse Problems*, Vol. 19, 279–295, 2003.

23. Cakoni, F., D. Colton, and H. Haddar, "The linear sampling method for anisotropic media," *J. Comp. App. Math.*, Vol. 146, 285–299, 2002.
24. Catapano, I., L. Crocco, and T. Isernia, "On simple methods for shape reconstruction of unknown scatterers," *IEEE Transactions on Antennas and Propagation*, Vol. 55, No. 5, 1431–1436, 2007.
25. Guzina, B., F. Cakoni, and C. Bellis, "On the multifrequency obstacle reconstruction via the linear sampling method," *Inverse Problems*, Vol. 29, 125005, 2010.
26. Catapano, I., F. Soldovieri, and L. Crocco, "On the feasibility of the linear sampling method for 3D GPR surveys," *Progress In Electromagnetics Research*, Vol. 118, 185–203, 2011.
27. Ambrosanio, M., M. Bevacqua, T. Isernia, and V. Pascazio, "Performance analysis of tomographic methods against experimental contactless multistatic ground penetrating radar," *IEEE Journal of Selected Topics in Applied Earth Observation and Remote Sensing*, Vol. 14, 1171–1183, 2021.
28. Catapano, I., L. Crocco, and T. Isernia, "Improved sampling methods for shape reconstruction of 3-D buried targets," *IEEE Transactions on Geoscience and Remote Sensing*, Vol. 46, No. 10, 3265–3273, 2008.
29. Cheney, M., "The linear sampling method and the MUSIC algorithm," *Inverse Problems*, Vol. 17, No. 4, 591–595, 2000.
30. Guo, Y., P. Monk, and D. Colton, "The linear sampling method for sparse small aperture data," *Applicable Analysis*, Vol. 95, No. 8, 1599–1615, 2016.
31. Haddar, H., A. Lechleiter, and S. Marmorat, "An improved time domain linear sampling method for Robin and Neumann obstacles," *Applicable Analysis*, Vol. 93, No. 2, 369–390, 2014.
32. Audibert, L. and H. Haddar, "The generalized linear sampling method for limited aperture measurements," *SIAM J. Imag. Sci.*, Vol. 10, No. 2, 845–870, 2017.
33. Kuo, Y.-H. and J.-F. Kiang, "Deep-learning linear sampling method for shape restoration of multilayered scatterers," *Progress In Electromagnetics Research C*, Vol. 124, 197–209, 2022.
34. Cakoni, F., M. Fares, and H. Haddar, "Analysis of two linear sampling methods applied to electromagnetic imaging of buried objects," *Inverse Problems*, Vol. 22, 845–867, 2006.
35. Burfeindt, M. and H. Alqadah, "Boundary-condition-enhanced linear sampling method imaging of conducting targets from sparse receivers," *IEEE Trans. Ant. Prop.*, Vol. 70, No. 3, 2246–2260, 2022.
36. Burfeindt, M. and H. Alqadah, "Qualitative inverse scattering for sparse-aperture data collections using a phase-delay frequency variation constraint," *IEEE Transactions on Antennas and Propagation*, Vol. 68, No. 11, 7530–7540, 2020.
37. Burfeindt, M. and H. Alqadah, "Qualitative inverse scattering from three-dimensional limited apertures using phase-delay frequency variation regularization," *Proc. IEEE Int. Symp. Ant. Prop. USNC-URSI Nat. Radio Sci. Meeting*, 1696–1697, 2022.
38. Burfeindt, M. and H. Alqadah, "Receive-beamforming-enhanced linear sampling method imaging," *Proceedings of the IEEE Research and Applications of Photonics in Defense (RAPID) Conference*, 2021.
39. Burfeindt, M. and H. Alqadah, "Phase-encoded linear sampling method imaging of conducting surfaces from full and limited synthetic apertures," *IEEE Open Journal of Antennas and Propagation*, Vol. 3, 1191–1205, 2022.
40. Burfeindt, M. and H. Alqadah, "Ground penetrating radar imaging via the linear sampling method under a phase-encoded formulation," *Proceedings of the IEEE Research and Applications of Photonics in Defense (RAPID) Conference*, 2022.
41. Balanis, C., *Advanced Engineering Electromagnetics*, Sec. 6.6, John Wiley and Sons, Hoboken, NJ, 1989.
42. Alqadah, H. and M. Burfeindt, "An adaptive monostatic inverse scattering approach using virtual multistatic geometries," accepted *Proc. IEEE Radar Conference*, 2023.
43. Akıncı M. N., M. Çayören, and I. Akduman, "Near-field orthogonality sampling method for microwave imaging: Theory and experimental verification," *IEEE Trans. Microw. Theory Techn.*, Vol. 64, No. 8, 2489–2501, 2016.

44. Leem, K. H., J. Liu, and G. Pelekanos, "Two direct factorization methods for inverse scattering problems," *Inverse Problems*, Vol. 34, No. 12, 125004, 2018.
45. Satopaa, V., J. Albrecht, D. Irwin, and B. Raghavan, "Finding a 'Kneedle' in a Haystack: Detecting knee points in system behavior," *Proc. Int. Conf. Dist. Comp. Sys. Workshops*, 2011.
46. Hansen, P. C., *Rank-Deficient and Discrete Ill-posed Problems*, Society for Industrial and Applied Mathematics, Philadelphia, 1998.
47. Crocco, L., I. Catapano, L. Di Donato, and T. Isernia, "The linear sampling method as a way to quantitative inverse scattering," *IEEE Transactions on Antennas and Propagation,* Vol. 60, No. 4, 1844–1853, 2012.
48. Palmeri, R., M. Bevacqua, L. Crocco, T. Isernia, and L. Di Donato, "Microwave imaging via distorted iterated virtual experiments," *IEEE Transactions on Antennas and Propagation*, Vol. 65, No. 2, 829–838, 2017.
49. Geffrin, J. and P. Sabouroux, "Continuing with the Fresnel database: experimental setup and improvements in 3D scattering measurements," *Inverse Problems*, Vol. 25, 024001, 1–18, 2009.